Modelling VARTM process induced variations on bending performance of composite Omega beams

Xuesen Zeng[1*], Peter Schubel[1], and Julien Lorrillard[2]

1. Composites Research Group, Faculty of Engineering, University of Nottingham, University Park, Nottingham, United Kingdom NG7 2RD
2. Aircelle Ltd, SAFRAN Group, Bancroft Road, Burnley, Lancashire, United Kingdom, BB10 2TQ

* Corresponding author. Tel.: +44 1159513820. E-mail address: xuesen.zeng@nottingham.ac.uk

Abstract

Finite element simulation with cohesive contact is presented, to correlate the vacuum assisted RTM process and the bending performance of Omega beams. The model considers the process induced variations, including part thickness, resin rich pockets and voids. The bending performance prediction relies on cohesive contact to model delamination initiation and propagation. Computing efficiency is achieved by mesh scaling. The modelling approach applies to three variations of Omega beams with the different mode-mixture ratios. The finite element predictions result in a high degree of agreement with the experimental measurements.

Keywords

B. Delamination; B. Defects; C. Cohesive interface modelling; E. Vacuum infusion

1. Introduction

Out-of-autoclave vacuum assisted resin transfer moulding (VARTM) poses challenges to produce aerospace graded composite structures. The associated quality variations include voids, resin rich pockets and varied thickness. The influence of these quality variations on the structural performance requires a close correlation, in order to prioritise and improve the

process parameters for aerospace applications. Delamination under out-of-plane bending load is one of major failure modes for composite laminates.

There have been extensive studies on the mechanisms of variations and defect formation during the VARTM processes. The strong coupling between the flexible vacuum bag pressure and the resin flow pressure led to non-uniform distribution of composite part thickness. The variation of pressure and compaction had further impact on formation of voids and resin rich pockets. Correia [1] was the first to propose a unified analytical model, for governing the material thickness coupled with the local pressure, compaction and permeability, as a function of infusion time and mould location. The analytical and experimental study demonstrated the VARTM process led up to 22% difference in the part thickness. The model was further verified experimentally by Yenilmez[2], showing the thickness variation of 7.5% based on their tests. Later, Park [3] derived the close-form analytical solutions for the evolution of part thickness, along with pressure, compaction stress, flow front and fibre volume fraction. Their results showed 15% variation of part thickness. Similarly, the numerical models were employed to simulate part thickness variation during the VARTM processes [4, 5].

Park [6] reviewed void formation and transport during liquid composite moulding processes. In most of cases, void formation was a result from the competition between the dual scale flows – capillary flow between fibre filaments and viscous flow between fibre tows. Specifically for the VARTM processes, Kuentzer [7] demonstrated experimentally and numerically that the void distribution was highly dependent on the extended resin bleeding time, additional flow resistance and flow medium. Kedari [8] highlighted the importance of reducing the inlet pressure to minimise the void content, while keeping the strong outlet vacuum to achieve the high fibre volume fraction.

Another practical issue in manufacturing complex parts was the inaccessible corners and fillets during the reinforcement preforming. It led to pressure bridging that affected local fibre volume fraction, thickness and resin rich pockets [9, 10].

Process and performance correlation was studied for VARTM processes experimentally. Li [11] compared the influence of two VARTM processes on part thickness, void and short beam shear strength. No conclusive correlation was established between the two processes. Mahdi [12] experimentally measured significant improvement of interfacial strength for the co-cured composite armour via VARTM, in comparison with the conventional bonded composite armour.

The numerical modelling approach was scarce in the literature, with the focus on VARTM process and structural performance correlation. This paper contributes to the literature on an efficient finite element modelling approach, in correlating the manufacture-induced defects with the experimentally observed performance variations. The experimental and numerical study focuses on composite Omega beams manufactured through a VARTM process as an example of an aero structure subcomponent. The correlation analysis is applied to four-point bending performance of Omega beams.

The proposed finite element model employed a cohesive zone method for modelling the delamination behaviour of an Omega beam under four-point bending. The cohesive zone method has been widely investigated for modelling composite delamination behaviour and was used for modelling fatigue delamination of composites [13], impact loading of UD laminate [14], compression after impact of UD laminate [15], soft impact of 3D woven composite [16], cantilever bending of 3D woven composites [17], and notched quasi-isotropic laminate under tension [18]. Turon [19, 20], Borg [21] and Harper [22] highlighted the sensitivity and the strategies in defining the cohesive properties.

Bertolini [23] successfully applied the cohesive zone method on modelling four-point bending performance of an Omega beam. The present study uses the similar load case with a distinct emphasis on modelling efficiency in order to correlate VARTM process and performance. This paper makes the following novel contributions to the literature of composite manufacturing research. The study has verified a simple mesh scaling strategy to improve the computing efficiency by three-fold. The proposed modelling approach has demonstrated good agreement with the experimental data, in correlating the process and performance. The method is a step closer towards process design and optimisation modelling for composite performance.

2. Specimen processing and test setup

An Omega beam is a typical sub-structure in aerospace applications. VARTM process was chosen as a low-cost route for manufacturing Omega stiffened laminate structures. In this study, the composite Omega beams were made from tri-axial non-crimp fabric (Hexcel HexForce) with two-part room temperature epoxy resin (Sicomin SR1710 and SD8824). Table 1 lists the key data for processing the fabric and the resin system. Figure 1 shows the schematic and actual setup of the VARTM process, which is a one-step process to infuse and co-cure the skin and the Omega beam. A silicone mandrel was used to preform the Omega stiffener during the VARTM process. Upon completing the post-cure, the silicone mandrel was manually withdrawn from the Omega beam. Both the skin and the stiffener contained two layers of tri-axial fabric with a measured fibre volume fraction of 0.55 ± 0.05. The stiffener had three variations of fabric lay-up, illustrated in Figure 1, referring to Omega 1, 2 and 3. Figure 2 shows the lay-up and dimensions of the corresponding Omega beam 1, 2 and 3.

The Omega beam samples were cut to 30 mm x 400 mm (width x length). Figure 3 shows the setup of the 4-point bending test, according to ASTM D 6272, ISO 14125 and the existing literature [23]. The tests were performed on a Instron 5969 with a 10KN load cell dual column mechanical tester. The Instron machine was calibrated by United Kingdom Accreditation Service. Three samples were tested for each of Omega beams 1, 2 and 3. The flexure displacement was recorded directly from the Instron crosshead, with the measurement accuracy of +/- 0.05% of the reading. As the maximum flexural displacement was up to 25 mm, the accuracy from the Instron crosshead was +/-0.0125 mm. The measurement accuracy for the flexural force was +/-0.5% of the reading.

3. Assessing the finite element model

3.1 Modelling setup

The finite element model was set up in ABAQUS/CAE. The geometric model, shown in Figure 4 (a), was created according to the dimensions in Figure 2. Both the moving rollers and the fixed rollers were simulated as rigid analytical shells. The rigid body motion for each roller was specified through the associated reference point (RP). The moving rollers (RP 1 and RP 2) travelled 25 mm along axis 2, while the fixed rollers (RP3 and RP4) had no displacement or rotation.

The contact constraint between the rollers and the Omega beam was enforced by the penalty contact algorithm with pure master-slave surface weighting. A linear response was imposed for the normal contact over-closure, with the penalty stiffness of 8.5 GPa equivalent to the transverse stiffness of the underlying composite lamina. The four point bending tests showed significant sliding between the Omega beam and the fixed rollers. Considering this experimental observation, the tangential contact response allowed frictional slippage between the rollers and the Omega beam. The frictional coefficient varied experimentally in the range

of 0.24 – 0.36 under the varied contact pressures at a sliding velocity of 2m/s [24]. The current study ran three FE analyses with the friction coefficients of 0.2, 0.3, and 0.5. The results suggested that the model was not sensitive to the selected values. Hence, the frictional coefficient was fixed to 0.3.

The reactional forces between the rollers and the Omega beam were generalised to the reference points. It allowed the post-processing to retrieve the deflection-force curve for the Omega beam through the reference points of the moving rollers (RP1 and RP2).

The model defined the consistent local coordinate systems for specifying the fibre orientations. There were two layers of non-crimp fabric for the skin and two layers for the Omega stiffener. The fabric has three UD laminas in $+30^o/90^o/-30^o$. Figure 4 (b) shows the inner fabric layer of the stiffener in Omega beam 3. The corner surfaces with curvatures were defined by a cylindrical coordinate system, while the flat surfaces were defined by a rectangular coordinate system. The spatial rotational angles $+30^o$, 90^o or -30^o for each lamina was specified along with the rotational axes: Z in the cylindrical coordinate system and Y in the rectangular coordinate system.

Figure 4 (c) shows the meshing strategy and the choice of element types for the current model. 3D continuum shell element (SC8R in ABAQUS notation) was chosen for the composite lamina, which was adopted for the similar applications in literature [23, 25]. The continuum orphan mesh was created through offsetting 2D shell mesh. The offset approach ensured mesh conformity, so that the initial contact surfaces were contacting without over-closure or separation. Three solid element layers were created to represent +30, 90, -30 composite laminas for each fabric layer.

The resin rich pockets were meshed into 8-node linear brick elements with reduced integration (C3D8R in ABAQUS notation). The analytical shells for the moving and fixed rollers used discreet rigid elements (R3D4 in ABAQUS notation).

Table 2 lists the material inputs for modelling the composite lamina and the cured resin. The resin properties were supplied by the manufacturer. For the composite lamina, the longitudinal modulus E_{11}along fibre direction was calculated by the rule of mixture based on the fibre volume fraction of 0.55. The modulus of the AS7 fibre and the resin were supplied in Table 1. The study adopted the remaining elastic properties from a similar composite lamina [23], except for the thickness-direction modulus E_{33}. As the composite lamina was modelled by continunn shell element, a stiff E_{33} resulted in very small time increment for the FE solution. E_{33} was numerically softened to 1 GPa, in order to improve the computing efficiency while maintaining the accuracy. More details on E_{33} are presented in Section 3.3, Mesh Scaling.

Table 2 lists the cohesive properties. Surface-based cohesive contact was used to simulate the progressive delamination in the Omega beams under four-point bending. In comparison with cohesive element method, cohesive contact was easier to implement and more versatile in modelling cohesive interaction. Both methods shared the similar traction-separation behaviour. Damage initiation of the cohesive contact was set according to the quadratic stress criterion, while damage evolution was governed by the energy based Benzeggagh-Kenane fracture criterion [26]. The normal and shear cohesive response were uncoupled and they followed the bi-linear traction-separation curves. The model assumed that the Omega beams approximately had the interfacial fracture energy of typical carbon fibre/epoxy composites. The previous experimental and numerical studies confirmed the fracture energy G_{Ic}in Mode I and G_{IIc} in Mode II were 260 J/m^2 and 1008 J/m^2 respectively [19, 21, 22, 27]. While the fracture energy was experimentally measurable as a material property, the cohesive strength

and the cohesive stiffness were considered mostly as the numerical parameters. The cohesive strength *N* for Mode I and *S* for Mode II/III were numerically determined as 40 MPa and 80 MPa respectively, based on the prediction fitting with the experimental measurements. Further discussion on the selection of cohesive strength will be in Section 3.3, Mesh Scaling. The appropriate cohesive stiffness was around $1x10^{14}$ N/m^3. In comparison, the default contact penalties in ABAQUS resulted in the same mechanical response prediction, whilst optimising the computing time. To simplify the cohesive specification, the model used the default contact penalties provided in ABAQUS instead of specifying the cohesive stiffness.

In addition to the inter-laminar cohesive behaviour, the model assigned a mode independent cohesive strength of 80 MPa for the resin rich pocket interface, which matches related literature [28].

3.2 Comparison with experimental data

A comparison of the numerical prediction and the experimental data for the load-displacement curves is shown in Figure 5. The finite element analyses involved the explicit dynamic solver in ABAQUS, together with the penalty contact algorithms between the rollers and the Omega beam. In comparison with ABAQUS/Implicit solver, ABAQUS/Explicit solver was more applicable in this study for taking into account shell element thickness in the contact penetration calculation. There was numerical noise in the predicted flexure load-displacement response. For consistency, the same Butterworth filter was applied, in the ABAQUS postprocessor, to the flexure load-displacement output for all the simulations. The set of filtered curves, based on the cohesive properties in Table 2, are noted as FE N=40, S=80 and R=80 MPa for Omega beams 1, 2 and 3. They are the benchmarking predictions. These results are in good agreement with the experiment, in terms of the initial linear slope, peak load and post-peak response. Table 3 lists the measured and predicted performance of

Omega beams 1, 2 and 3 under the four point bending test. Experimentally, Omega beam 1 achieved the highest peak load, doubling that of Omega beam 2 and 30% higher than Omega beam 3. The standard deviation in the experiment was consistent with our further tests on the different Omega beam designs. The numerical model closely captured these different performances amongst the three beams. The discrepancy between the prediction and the average measurement was 8% (Omega beam 1), 10% (Omega beam 2) and 3% (Omega beam 3).

The FE analyses resulted in the realistic predictions of the progressive delamination and the overall deformation (Figure 6). Typically, the delamination was not symmetrical on the left and right side of the omega beam cross-section. This was because the fibre orientations, +30/90/-30 degrees in the tri-axial fabric, were not symmetrical to the left and right sides of Omega beam cross-section. Visible for Omega beam 1 and 2 in Figure 6, the right side of the cross-section delaminated first and progressed further than the left side. The FE model closely captured the sequence and the length of the delamination.

Figure 5 also includes the FE predictions, using the isotropic cohesive strength of Mode I or II. These curves demonstrate the numerical sensitivity of damage initiation to the mode mixture. The mix-mode delamination in Omega beam 1 was closer to the pure Mode II than Mode I. Omega beam 3 was close to the pure Mode I fracture. The fracture mode for Omega 2 was halfway between Mode I and Mode II (Figure 5). From the FE result, the stress mode-mixture ratio ($\emptyset_m$) for cohesive contact was calculated by

$$\emptyset_m = \frac{2}{\pi}\tan^{-1}\frac{\tau_{sh}}{\tau_n}, \qquad (1)$$

where τ_{sh} and τ_n are the effective shear stress and the normal stress on cohesive contact interface. At the locations of crack initiation indicated by arrows in Figure 6, the calculated mode-mixture ratio was 0.70 (Omega beam 1), 0.50 (Omega beam 2) and 0.26 (Omega beam

3). The mode-mixture ratio correlates well with the observation in Figure 5 on the sensitivity of load-extension responses to the mix-mode cohesive strength.

3.3 Mesh scaling

The processing time was 14 hours for each analysis reported above, using seven Intel i7 960 3.20 GHz CPUs in parallel. Such computing cost is typically not viable in industrial applications. In many cases, an optimisation procedure in design and manufacturing of composite structures would demand a large number of iterations of FE analyses. Therefore, it is desirable to maximise the computing efficiency while maintaining reasonable numerical accuracy.

One possible approach is to use a coarser mesh with scaling the relevant numerical parameters. The cohesive behaviour could be preserved by adapting the cohesive strength in Mode I (N) and in Mode II (S). The current study simplified the existing scaling strategies in literature [19, 22], for Mode I

$$N_2 = N_1\sqrt{\frac{l_1}{l_2}} \quad (2)$$

and for Mode II

$$S_2 = S_1\frac{l_1}{l_2}, \quad (3)$$

where $N_1$and S_1 are the cohesive strength set for the mesh size l_1, whilst N_2 and S_2 are for the mesh size l_2. Element sizes l_1 and l_2 refer to the average element size specified for every edge of the Omega beams. The resulted element size was approximately uniform over the entire part, except curvature-controlled adjustment at the stiffener corners. There was no mesh refinement or mesh adaption along the debonding direction. The cohesive strength R for the interface of resin rich pocket was assumed to follow the same scaling factor as in Eq. 3.

The through-thickness stiffness E_{33} of continuum shell element was critical for computing time and numerical stability. It showed no significant influence on the bending rigidity, based on our parametric study by changing E_{33} alone. The scaling of the through-thickness stiffness followed

$$E_{33}|_2 = E_{33}|_1 \left(\frac{l_1}{l_2}\right)^2. \quad (4)$$

In order to simulate the quasi-static loading condition, the model kept the kinetic energy less than 2% of the strain energy throughout the analyses. The minimum time step (T) for the explicit dynamic analysis was scaled according to

$$T_2 = T_1\sqrt{\frac{l_1}{l_2}}. \quad (5)$$

The mesh scaling from mesh size 1 mm to 1.5 mm and 2 mm was applied to Omega beams 1, 2 and 3. Table 4 lists the scaled numerical parameters according to Equation 2 – 5. The computing time reduced from 14 hours to 5 hours, when the mesh size increased from 1 mm to 2 mm, providing a 3-fold reduction in computing efficiency.

Figure 7 plots the predicted flexure load-extension response based on the mesh size of 1 mm, 1.5 mm and 2 mm. For all of Omega beams 1, 2 and 3, the different mesh size did not result in deviation on the initial load-extension slope, suggesting that the chosen mesh sizes were converged in terms of the linear elastic response of the Omega beams. The mesh sensitivity study without the scaling procedure showed the same convergence in bending rigidity. It also indicated that the scaled through-thickness stiffness E_{33} did not influence the bending rigidity.

The scaled models resulted in the closely predicted peak force, with a standard deviation of 13% (Omega 1), 5% (Omega beam 2) and 3% (Omega beam 3). The simulation results suggest that the mesh scaling approach is effective to improve computing efficiency and maintain acceptable accuracy. The scaling approach did lead to difference in predicting the

onset and propagation of delamination. However, the level of accuracy was adequate for the manufacturing design analysis. The scatter of the post-peak prediction was well within the upper and lower bounds of the experimental measurements. The exact cause of post-peak deviation requires further investigation.

Previous findings suggested that the accurate representation of cohesive damage required at least three elements ahead of the crack tip [19, 22]. Figure 8 illustrates the effect of scaling the cohesive strength parameters. For the varied mesh size in the current study, the scaled cohesive strength ensured there were always approximately three elements within the softening zone ahead of the delamination.

3.4 Modelling manufacture induced deviations

The 4-point bending experimental data in Table 3 and Figure 5 showed significant variation from sample to sample within each Omega beam design. The flexural stiffness varied by 30% on average and the peak force varied by 15% on average. The most likely sources of variation can be traced back to the VARTM process. Characterisation of the Omega beams showed that the laminate thickness was 1.7 ± 0.1 mm. A coarse mesh model with an element size of 2 mm was used to simulate Omega beam 1 with skin thicknesses of 1.8 mm, 1.7 mm and 1.6 mm. The numerical results in Figure 9 showed that the bending stiffness increased by 28% from for a skin thickness of 1.6 mm to 1.8 mm. The influence of beam thickness on bending stiffness could be explained by the classic linear elastic beam theory. The bending stiffness is in proportion to cubic of beam thickness. Theoretically, a 10% increment in the beam thickness would lead to 33% increment in bending stiffness.

Figure 10 shows the other two common defects associated with the VARTM process. The arrows in Figure 10a highlight the resin rich noodles at the sharp corners of Omega stiffener.

The VARTM process relied on the flexible vacuum bag for forming the Omega feature, requiring significant effort to minimise the resin rich pockets. The influence of the resin noodles on 4-point bending performance was modelled explicitly, shown in Figure 10a, with inclusion of 2 noodles, 1 noodle or no noodle. The predictions in Figure 11 suggested that the bending stiffness increased by 12% due to one additional noodle, and by 24% due to two noodles. The peak load increased by 4% and 8% due to one and two additional noodle(s) respectively.

The arrows in Figure 10b indicate voids within the skin of Omega beam 1. The image was acquired through x-ray micro computed tomography. The exact association between delamination and void distribution was not within the scope of the current study, because it would require further work to determine the relationship between the cohesive behaviour and void content. A qualitative speculation was possible in the current study, by downgrading the cohesive strength to reflect the void content at the cohesive zone. In Figure 5, when the cohesive strength was halved, the peak load dropped by 30% for both Omega beams 1 and 2.

4. Conclusions

The experimental and numerical study has focused on composite Omega beams as an example of an aero structure subcomponent. Three variations in Omega stiffener layup were investigated. The four-point bending tests revealed that the layup variations had significant influence on the bending performance of the Omega beams. The experiments also demonstrated large scatter in bending stiffness by 30% and bending strength by 15% within the samples from the same Omega layup. The numerical study later confirmed the correlation of this scatter to the variation in void, resin rich pockets and thickness in the Omega beams.

The finite element model employed continuum shell elements for representing individual lamina. Cohesive zone contact was applied to model the delamination behaviour between laminas and the interface between a resin rich pocket and laminas. By comparing mesh size 1mm, 1.5mm and 2 mm, the study found that the coarse mesh was accurate and effective, provided the numerical cohesive strength was adapted. For all three Omega layups, the finite element model showed strong correlated with experimental data for the entire load-displacement curve and the delamination configurations. After the validation, the model further incorporated the separate changes in resin pocket, thickness and void. The predicted bending performances matched well with the scatter observed in the experiments. The devised modelling method has been shown to provide a robust approach for composite processing towards better structural performance.

Acknowledgement

The work was funded by the Department of Business, Innovation and Skills – United Kingdom, through the Advanced Manufacturing Supply Chain Initiative Project 510929.

References

[1] Correia N, Robitaille F, Long A, Rudd C, Šimáček P, Advani S. Analysis of the vacuum infusion moulding process: I. Analytical formulation. Composites Part A: Applied Science and Manufacturing. 2005;36(12):1645-56.
[2] Yenilmez B, Senan M, Sozer EM. Variation of part thickness and compaction pressure in vacuum infusion process. Composites Science and Technology. 2009;69(11):1710-9.
[3] Park CH, Saouab A. Analytical modeling of composite molding by resin infusion with flexible tooling: VARI and RFI processes. Journal of Composite Materials. 2009; 43(18):1877-1900.
[4] Govignon Q, Bickerton S, Kelly P. Simulation of the reinforcement compaction and resin flow during the complete resin infusion process. Composites Part A: Applied Science and Manufacturing. 2010;41(1):45-57.
[5] Correia N, Robitaille F, Long A, Rudd C, Simacek P, Advani SG. Use of resin transfer molding simulation to predict flow, saturation, and compaction in the VARTM process. Journal of fluids engineering. 2004;126(2):210-5.
[6] Park CH, Lebel A, Saouab A, Bréard J, Lee WI. Modeling and simulation of voids and saturation in liquid composite molding processes. Composites Part A: Applied Science and Manufacturing. 2011;42(6):658-68.

[7] Kuentzer N, Simacek P, Advani SG, Walsh S. Correlation of void distribution to VARTM manufacturing techniques. Composites Part A: Applied Science and Manufacturing. 2007;38(3):802-13.
[8] Kedari VR, Farah BI, Hsiao K-T. Effects of vacuum pressure, inlet pressure, and mold temperature on the void content, volume fraction of polyester/e-glass fiber composites manufactured with VARTM process. Journal of Composite Materials. 2011;45(26):2727-42.
[9] Ma Y, Centea T, Nutt SR. Defect reduction strategies for the manufacture of contoured laminates using vacuum BAG‐only prepregs. Polym Composite. 2015. DOI: 10.1002/pc.23773
[10] Levy A, Stadlin J, Pascal H. Corner Consolidation in Vacuum Bag Only Processing of Out-of-Autoclave Composite Prepregs Laminates. SAMPE 2014 Technical Conference, Seattle2014.
[11] Li W, Krehl J, Gillespie J, Heider D, Endrulat M, Hochrein K, et al. Process and performance evaluation of the vacuum-assisted process. Journal of Composite Materials. 2004;38(20):1803-14.
[12] Mahdi S, Gama BA, Yarlagadda S, Gillespie Jr JW. Effect of the manufacturing process on the interfacial properties and structural performance of multi-functional composite structures. Composites Part A: Applied Science and Manufacturing. 2003;34(7):635-47.
[13] Jimenez S, Duddu R. On the parametric sensitivity of cohesive zone models for high-cycle fatigue delamination of composites. International Journal of Solids and Structures. 2016;82:111-24.
[14] Zhang J, Zhang X. Simulating low-velocity impact induced delamination in composites by a quasi-static load model with surface-based cohesive contact. Composite Structures. 2015;125:51-7.
[15] Dang TD, Hallett SR. A numerical study on impact and compression after impact behaviour of variable angle tow laminates. Composite Structures. 2013;96:194-206.
[16] Turner P, Liu T, Zeng X. Dynamic Response of Orthogonal Three-Dimensional Woven Carbon Composite Beams Under Soft Impact. Journal of applied mechanics. 2015;82(12):121008-.
[17] Turner P, Liu T, Zeng X. Collapse of 3D orthogonal woven carbon fibre composites under in-plane tension/compression and out-of-plane bending. Composite Structures. doi:10.1016/j.compstruct.2016.01.100
[18] Xu X, Wisnom MR, Li X, Hallett SR. A numerical investigation into size effects in centre-notched quasi-isotropic carbon/epoxy laminates. Composites Science and Technology. 2015;111:32-9.
[19] Turon A, Dávila CG, Camanho PP, Costa J. An engineering solution for mesh size effects in the simulation of delamination using cohesive zone models. Engineering Fracture Mechanics. 2007;74(10):1665-82.
[20] Turon A, Camanho PP, Costa J, Renart J. Accurate simulation of delamination growth under mixed-mode loading using cohesive elements: Definition of interlaminar strengths and elastic stiffness. Composite Structures. 2010;92(8):1857-64.
[21] Borg R, Nilsson L, Simonsson K. Modeling of delamination using a discretized cohesive zone and damage formulation. Composites Science and Technology. 2002;62(10–11):1299-314.
[22] Harper PW, Hallett SR. Cohesive zone length in numerical simulations of composite delamination. Engineering Fracture Mechanics. 2008;75(16):4774-92.
[23] Bertolini J, Castanié B, Barrau J-J, Navarro J-P. An experimental and numerical study on omega stringer debonding. Composite Structures. 2008;86(1–3):233-42.
[24] Suresha B, Chandramohan G, Samapthkumaran P, Seetharamu S, Vynatheya S. Friction and Wear Characteristics of Carbon-epoxy and Glass-epoxy Woven Roving Fiber Composites. Journal of Reinforced Plastics and Composites. 2006;25(7):771-82.
[25] Ridha M, Tan VBC, Tay TE. Traction–separation laws for progressive failure of bonded scarf repair of composite panel. Composite Structures. 2011;93(4):1239-45.
[26] Kenane M, Benzeggagh M. Mixed-mode delamination fracture toughness of unidirectional glass/epoxy composites under fatigue loading. Composites Science and Technology. 1997;57(5):597-605.
[27] Choupani N. Mixed-mode cohesive fracture of adhesive joints: Experimental and numerical studies. Engineering Fracture Mechanics. 2008;75(15):4363-82.

[28] Joosten MW, Dingle M, Mouritz A, Khatibi AA, Agius S, Wang CH. A hybrid embedded cohesive element method for predicting matrix cracking in composites. Composite Structures. 2016;136:554-65.

Table 1. Reinforcement and matrix properties

Reinforcement	
Tri-axial fabric	+30/90/-30
Weight per layer (g/m^2)	267
Nominal weight (g/m^2)	801
Yarn	AS7 GS-12K filaments
Yarn weight (g/m)	0.8
Fibre diameter (µm)	6.9
Fibre density (g/cm^3)	1.79
Fibre tensile strength (GPa)	4.895
Fibre modulus (GPa)	248
Stitch yarn	Polyester
Binding powder	Epoxy E01 5 gsm on one side
Fabric thickness at 55% of fibre volume fraction (mm)	0.85
Matrix (Epoxy resin/hardener)	Sicomin SR1710 / SD8824
Mixing ratio by weight	100 g / 36 g
Mixing ratio by Volume	100 ml / 43 ml
Viscosity of the mix at 20 ^{o}C (Pa·s)	0.55
Cure cycle	20 hours at 20 ^{o}C
Post cure	16 hours at 60 ^{o}C
Cured density (g/cm^3)	1.17

Table 2. Cured composite properties and cohesive properties in the simulation

Lamina properties		Resin properties		Lamina cohesive properties	
E_{11} (GPa)	137	E (GPa)	2.78	G_{Ic} (J/m^2)	260
E_{22} (GPa)	8.50	v	0.30	$G_{IIc} = G_{IIIc}$ (J/m^2)	1008
E_{33} (GPa)	1.00	ρ (kg/m^3)	1170	N (MPa)	40
$G_{12} = G_{13}$ (GPa)	4.50			S (MPa)	80
G_{23} (GPa)	3.22			Resin rich pocket cohesive properties	
$v_{12} = v_{13} = v_{23}$	0.32			R (MPa)	80
ρ (kg/m^3)	1510			η	2

Table 3. Experimental and numerical data of Omega beam performance under 4-point bending

	Max flexure stress (MPa)	Max load (N)	FE Max load (N)	Error
Omega beam 1	525.99 ± 64.28	380.03 ± 46.44	350	-8%
Omega beam 2	247.07 ± 26.29	178.51 ± 19.00	160	-10%
Omega beam 3	427.13 ± 75.49	290.10 ± 45.82	300	+3%

Table 4. Mesh scaling settings

Mesh size (mm)	Number of element (x10^3)	N (MPa)	S, R (MPa)	E_{33} (GPa)	Time step (seconds)	CPU time (hours)
1	92	40	80	1	56	14
1.5	43	33	60	0.44	45	8.5
2	25	30	40	0.25	40	5

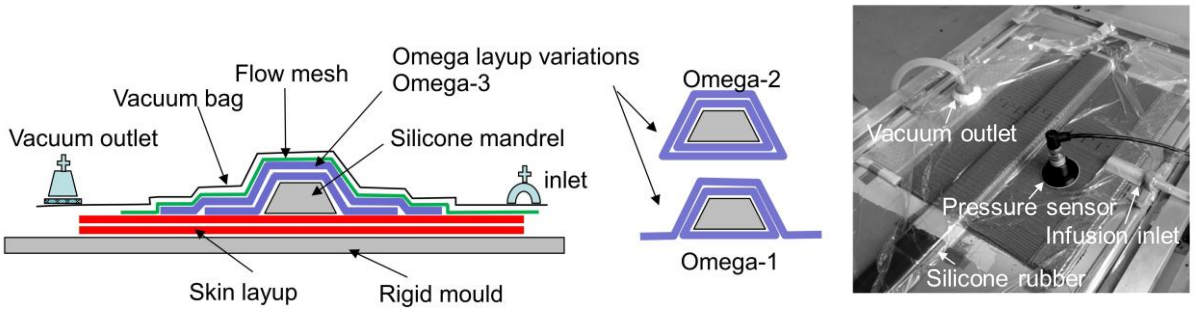

Figure 1. Sketch (Left) and actual setup (Right) of vacuum assisted resin transfer moulding for manufacturing Omega beam 1, 2 and 3

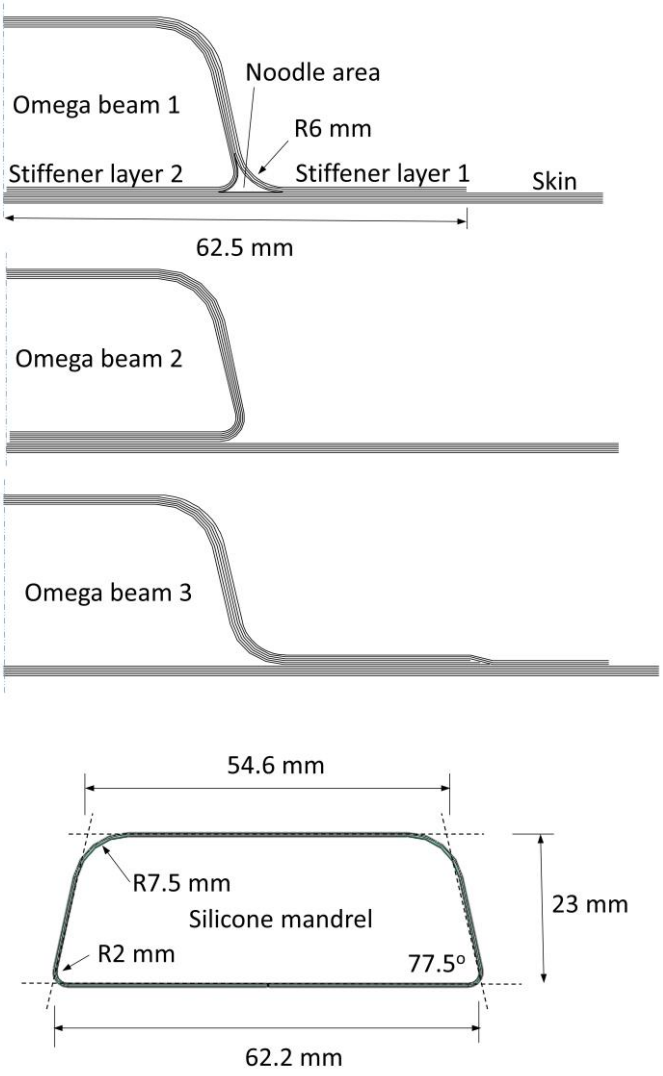

Figure 2. Lay-up designs and feature dimmensions for manufacturing Omega beam 1, 2 and 3

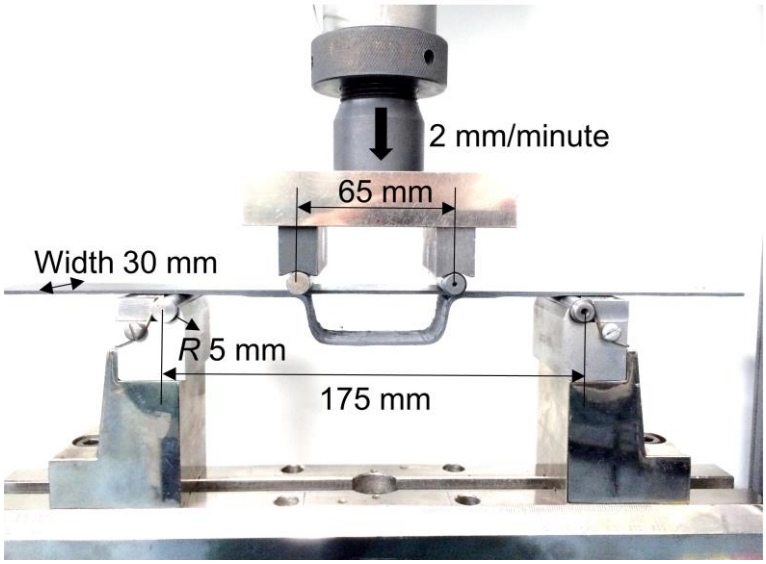

Figure 3. Four point bending test setup

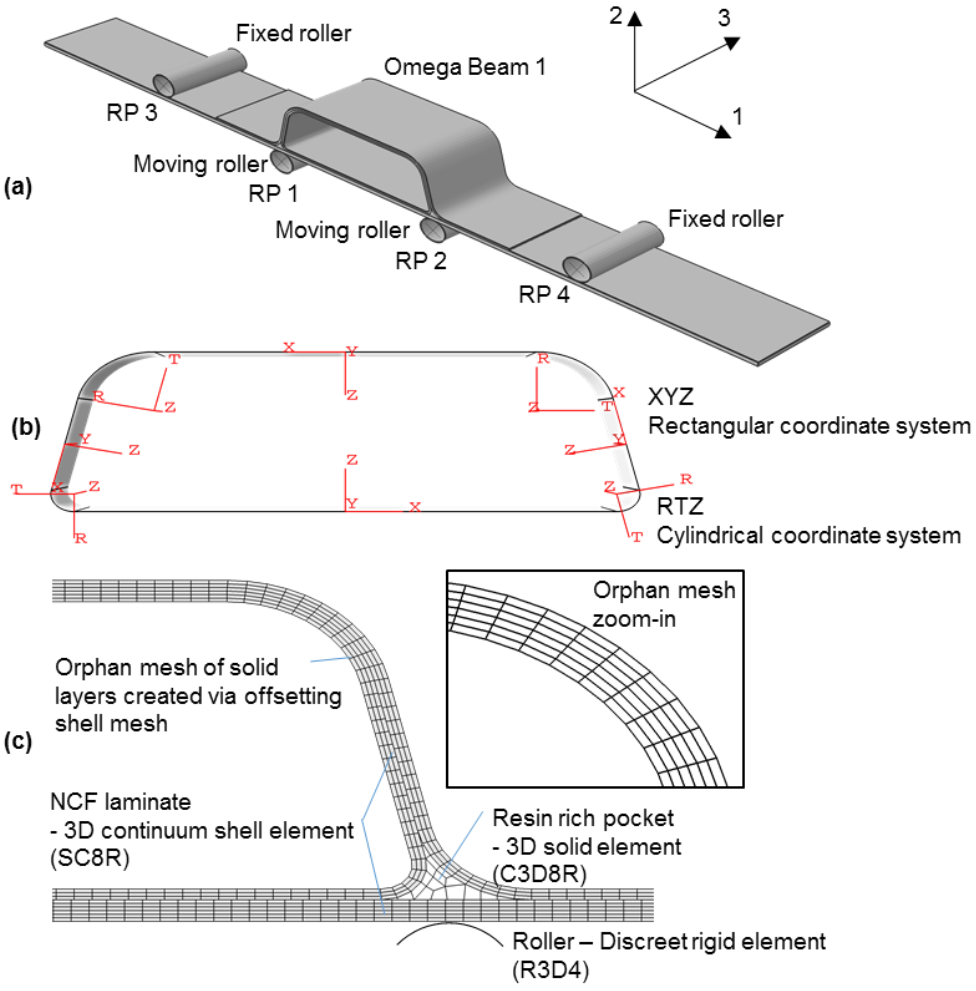

Figure 4. Implementation of the finite element model: (a) Overall geometric representation of 4-point bending test; (b) Example of local coordinate systems for defining fibre orientations; (c) Meshing strategy with the element types in ABAQUS notation.

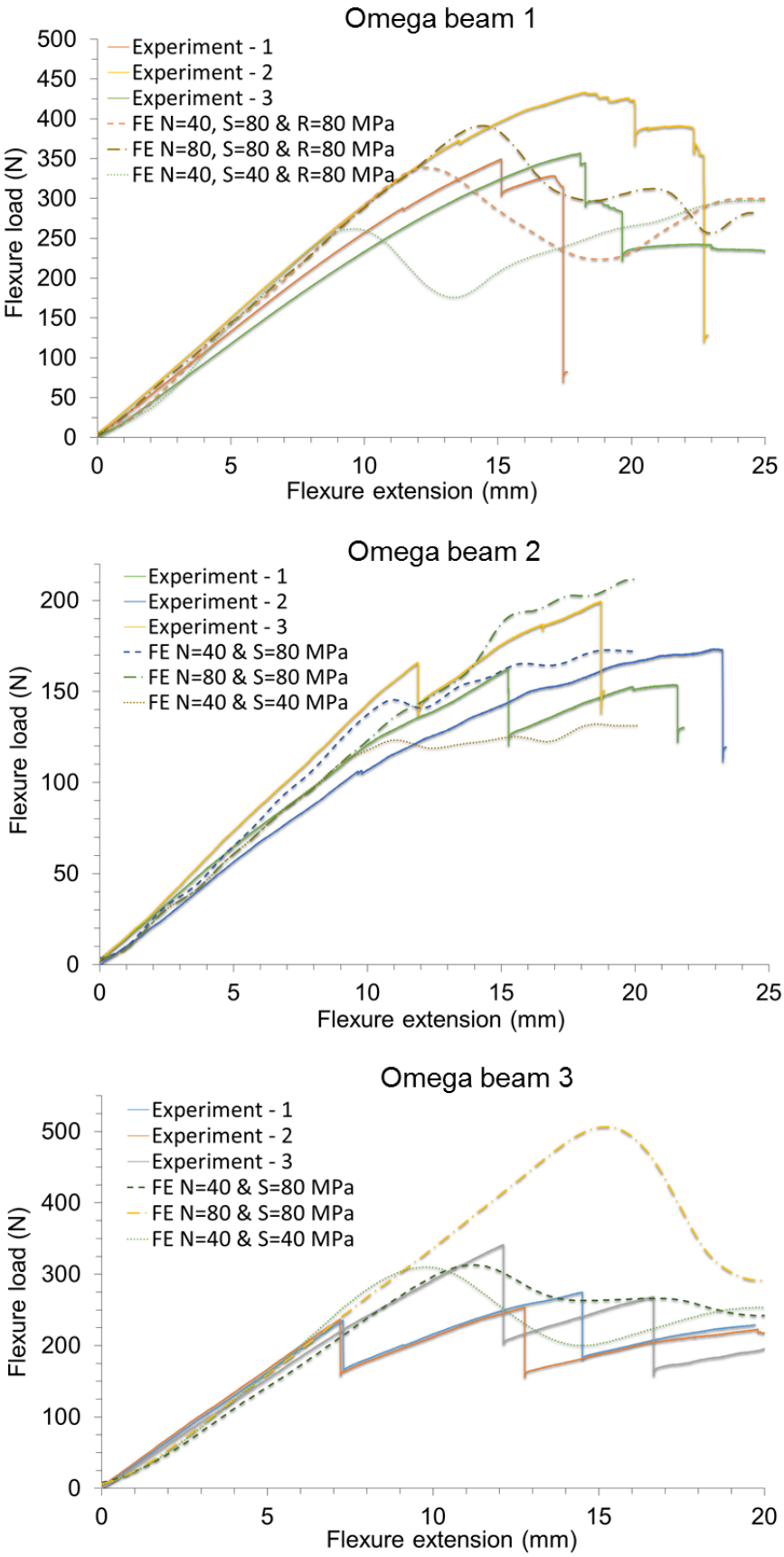

Figure 5. Curves of flexure load vs flexure extension from experiment and FE prediction.

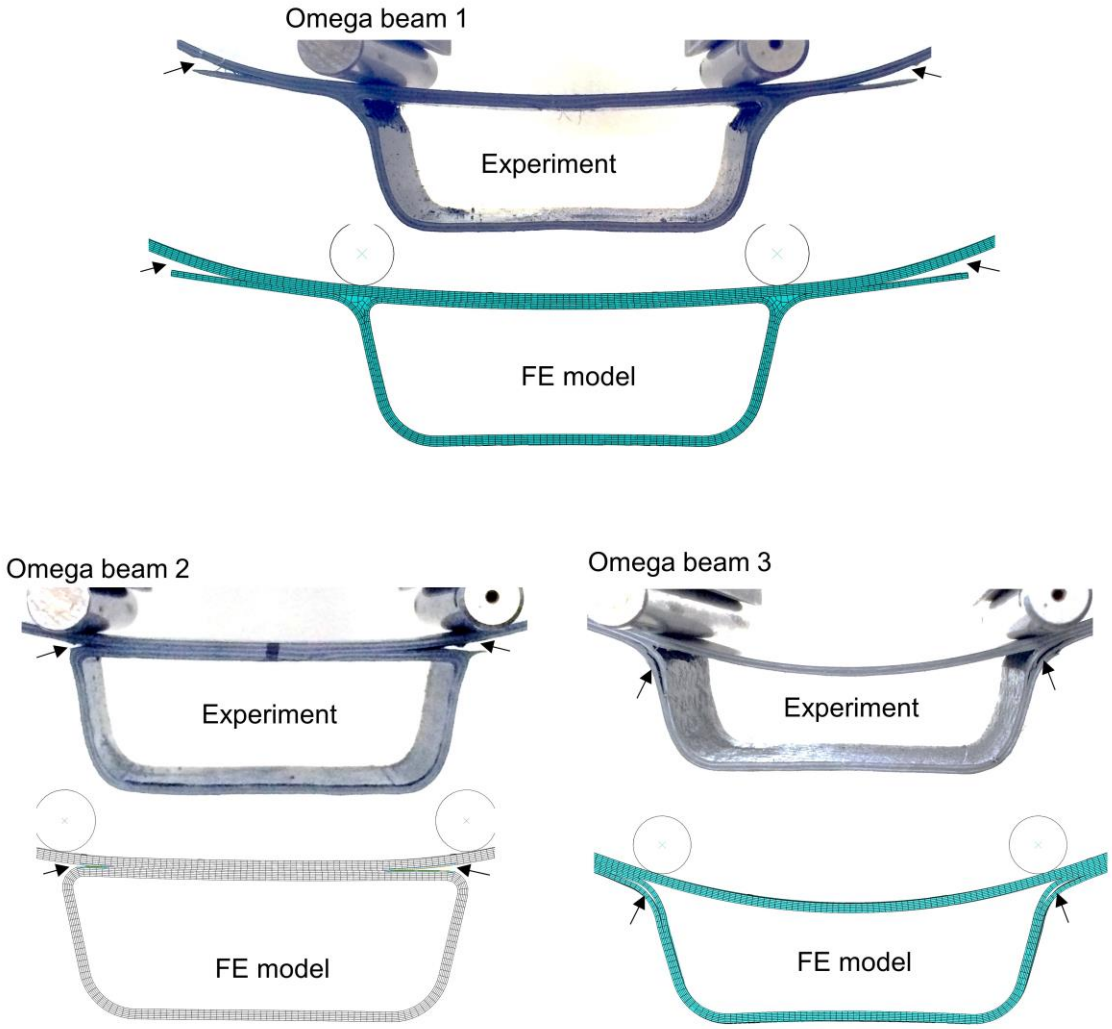

Figure 6. Comparing delamination progression between the experiment and the FE prediction (N=40, S=80 & R=80 MPa), with the arrows pointing to the delamination spots.

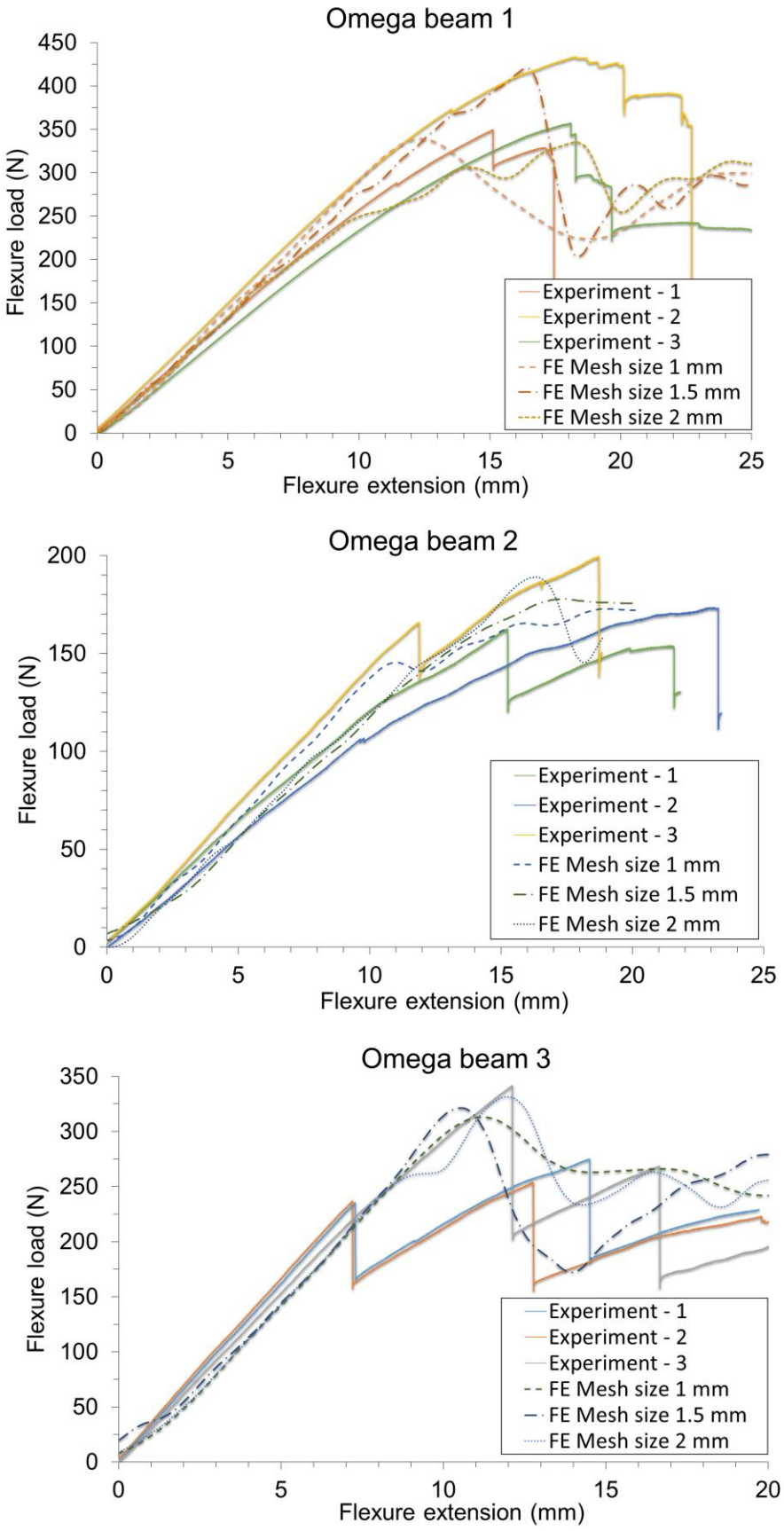

Figure 7. Numerical predictions based on the mesh size 1 mm, 1.5 mm and 2 mm with the scaling of cohesive parameters, in comparison with the experimental measurements.

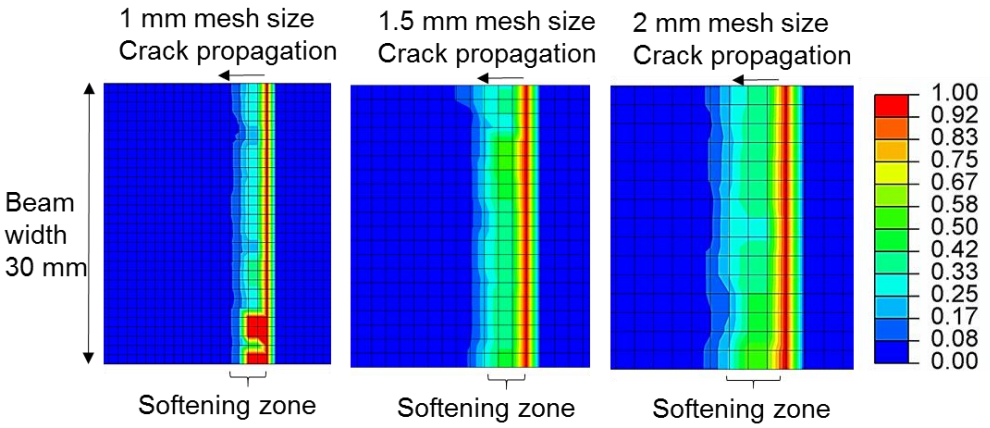

Figure 8. Contour plot of the quadratic cohesive damage initiation criterion with the mesh size 1 mm, 1.5 mm and 2 mm for Omega beam 1, showing approximately 3 elements within the softening zone (Colour band, 1: failure initiation, 0 < otherwise <1: cohesive softening).

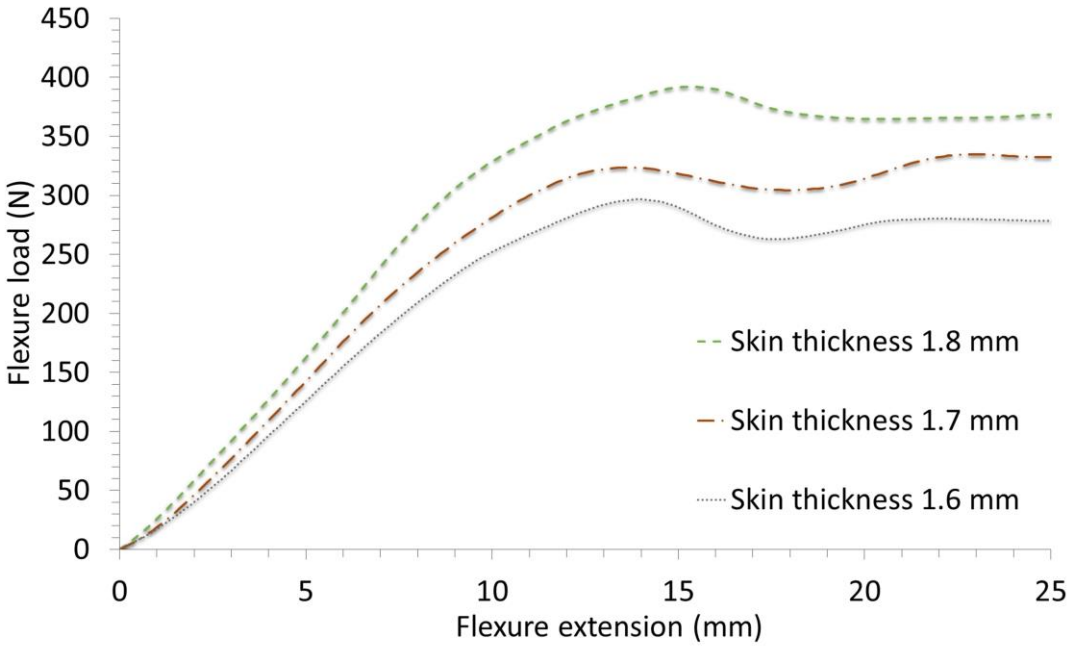

Figure 9. Influence of skin thickness on the 4-point bending performance of Omega beam 1.

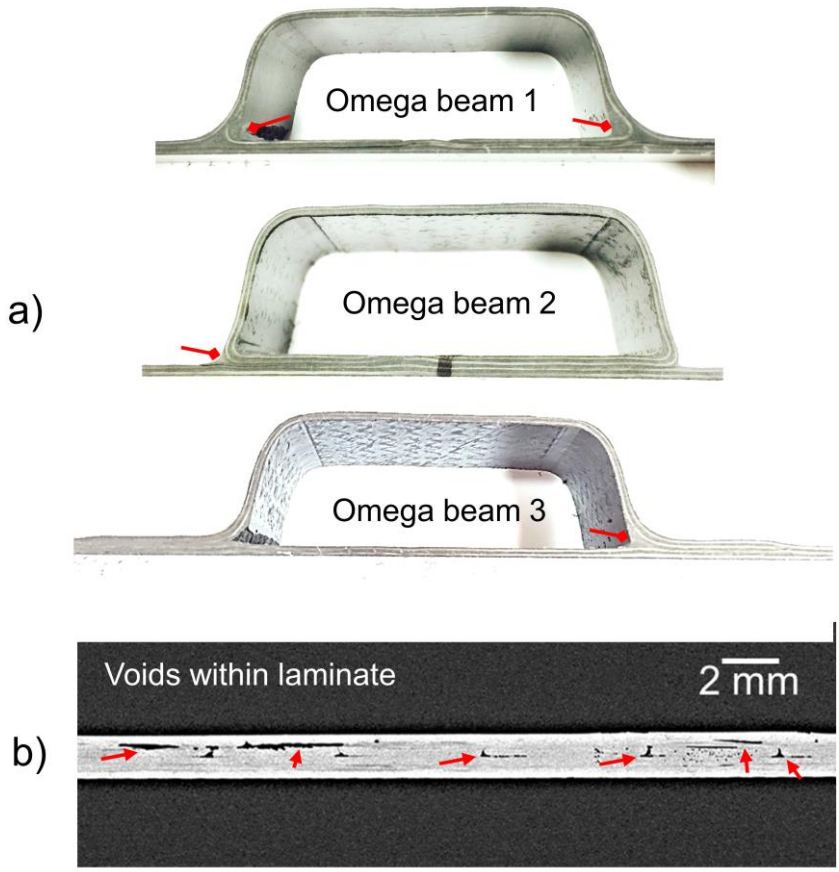

Figure 10. Photographic evidence of manufacture induced defects: a) Diamond arrows pointing to resin rich noodles; and b) normal arrows pointing to voids within laminate.

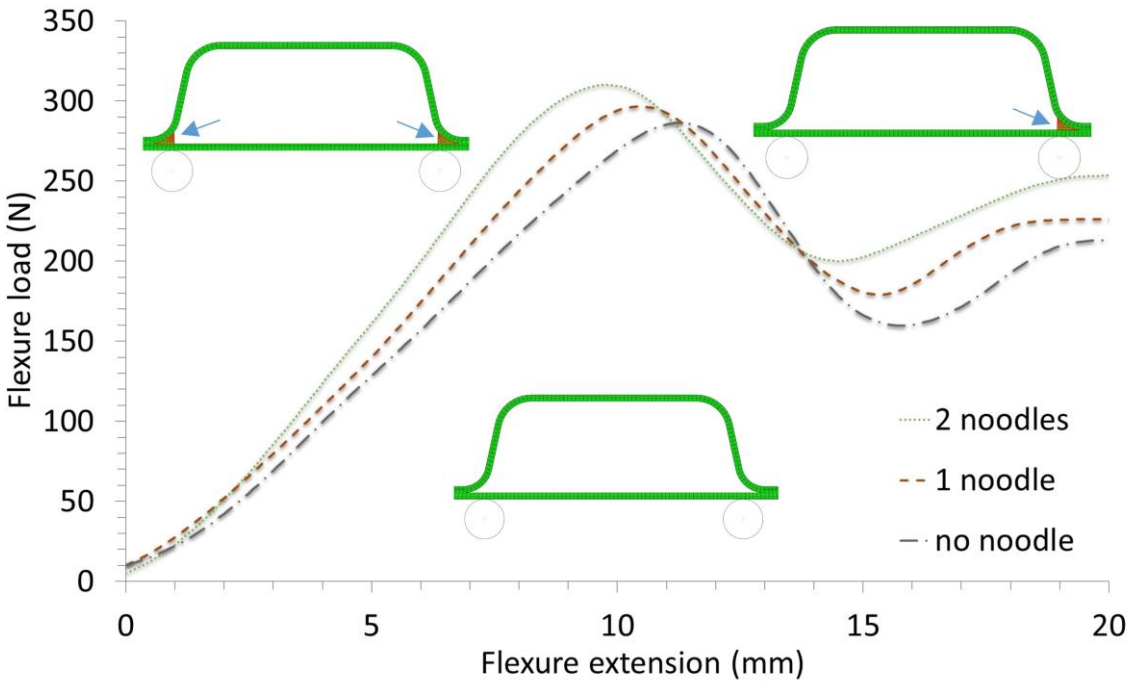

Figure 11. Influence of resin rich noodles on the 4-point bending performance of Omega beam 3.